UNIVERSITAT DE BARCELONA

A study of the shortwave schemes in the Weather Research and Forecasting model

Alex Montornès Torrecillas

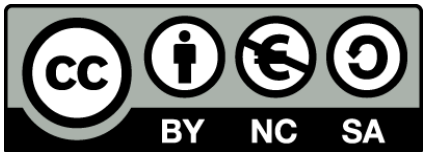

Chapter 6

Study of the physical error under clear-sky conditions

In the previous chapter, errors associated with the model vertical settings have been analyzed by means of the truncation and the TOM errors. The method was based on the sandbox tool described in Sect. 4.2 and providing different ideal vertical profiles as input data-sets.

Ideal vertical profiles were a powerful tool for discussing the impact of the vertical settings on the outcomes because they were flexible and hence, a wide range of vertical configurations covering from tens to thousands of vertical levels, equidistantly and logarithmically distributed and with several TOM values could be tested. Nevertheless, those profiles were unrealistic, limiting the discussion of the physical errors introduced in the treatment of the radiative transfer.

In the current chapter, the physical error, ϵ_{phys} will be studied under cloudless conditions. To do that, ideal profiles are laid apart and they are substituted by real soundings provided by the Integrated Global Radiosonde Archive data-set located in sites where ground-based measurements are available, particularly, from the Baseline Surface Radiation Network.

Therefore, by assuming that the measured vertical profile is representative of the vertical atmospheric column, the outcomes for each parameterization can be compared with the real data, leading to an estimation of ϵ_{phys}.

First of all, the methodology used for the study of the physical error is described in Sect. 6.1. The analysis includes a robust validation of the surface fluxes presented in Sect. 6.2 and a discussion about the differences on the vertical profiles in the fluxes as well as in the heating rate, in Sect. 6.3.

6.1 Methodology

The physical error is evaluated running the sandbox tool in a set of sites using real vertical profiles provided by real soundings as input data-sets. The outcomes of the solar schemes are validated comparing with ground-based irradiance measurements at the same or nearby location in the available period at each site. In this section, the procedures and assumptions leading to the results presented in Sects. 6.2 and 6.3 will be described.

The experiments are performed at sites from the BSRN (Ohmura et al., 1998). This data-set is appropriate for the purposes of this chapter because it provides a large number of stations at different climate regions with the best possible quality for shortwave and longwave surface radiation fluxes. Moreover, some of these sites also provide vertical and surface meteorological measurements mandatory for these experiments as it was exposed in Sect. 4.2. The choice of sites is based on three conditions related with the data availability: i) BSRN sites should have a valid sounding station at the same place for the concurrent period of the radiative measurements, ii) one of the two launching times (i.e. 00 or 12 UTC) must be performed in

a clear daytime period and iii) surface weather measurements must be available at the same place for the same period.

First and third conditions are necessary for creating the input data for the radiative codes. The second requirement excludes all stations located in America and Central Asia because radiosoundes are launched during the local night or during the local sunrise/sunset in some periods of the year, when the solar zenith angle is too large and scattering and shadow effects can distort the discussion.

In virtue of these specifications, a subset of six stations are used in this study (Table 6.1): Georg von Neumayer (Antarctica), Lindenberg (Germany), Payerne (Switzerland), Sappore (Japan), Syowa (Antarctica) and Tamanrasset (Algeria). Although the questionable usefulness of the results at the polar sites for solar industry applications, these sites have been selected because Antarctica is the region of the world with the lowest contribution of the continental aerosols as it was discussed by previous authors as Wagenbach et al. (1988), Obleitner (1992) or König-Langlo and Loose (2007), among others. Therefore, these sites experience a low turbidity and they can be used in the analysis of the behavior of the solar schemes in a extremely clear-sky (i.e. without aerosols) atmosphere.

Table 6.1: BSRN stations used in this study

Label	Name	Latitude [deg]	Longitude [deg]	Elevation [m]	Sounding station	Sounding time [UTC]
TAM	Tamanrasset	22.7903	5.5292	1385	60680	12
GVN	Georg von Neumayer	-70.6500	-8.2500	42	89002	12
SYO	Syowa	-69.0050	39.5890	18	89532	12
LIN	Lindenberg	52.2100	14.1220	125	10393	12
PAY	Payerne	46.8150	6.9440	491	06610	12
SAP	Sappore	43.0600	141.3283	7	47412	00

Following the recommendations provided by the BSRN program (Long and Dutton, 2002), all real radiative fields have been revised using a two part control study. Firstly, GHI, DHI and DIF are filtered by using a set of possible physical limits. The lowest allowed value in all these fields is set to -4 W m^{-2}, while the upper limit is set to $(1.50 S_0 \mu_0^{1.2} + 100)$, S_0 and $(0.95 S_0 \mu_0^{1.2} + 50)$ W m^{-2}, respectively, being S_0 and μ_0 the solar constant and the cosine of the solar zenith angle. Secondly, these radiative fields are compared one to each other, in search of physical inconsistencies. Regarding the GHI, the ratio $GHI/(DHI + DIF)$ cannot exceed a specific threshold while for DIF, we the ratio DIF/GHI is used. Further information about these thresholds is available in Long and Dutton (2002).

Although the BSRN's server contains raw data for the vertical soundings at all the selected sites, soundings from the IGRA data-set (Elliott and Gaffen, 1991) are used. This data-set provided by the National Oceanic and Atmospheric Administration (NOAA) consists of pilot balloon and radiosonde observations for more than 1500 globally distributed stations with a period that generally extends from 1970 to present. Measurements are available at different levels (standard, surface, tropopause and significant levels) and variables include pressure, temperature, geopotential height, dew point depression, wind direction, and wind speed. These data-sets are checked with different quality controls to ensure the temporal and spatial homogeneity. Consequently, data from IGRA ensure more reliable results in our experiments than using directly the data provided by the BSRN stations.

Nevertheless, the IGRA data-set is not directly compatible with the specifications of the

solar parameterizations and hence, pre-processing stage is needed before launching the experiments. Particularly, the geometric height z from surface and the water vapor mixing ratio q_v are two variables required by the solar schemes but not provided in the IGRA files.

The geopotential ϕ is converted to geometric height z considering the gravity variation with height as shown in NASA (1976) and described in Eq. 5.3. Although this correction introduces a small improvement for the typical heights achieved by soundings, this approach to the problem homogenizes the process with respect to the case of ideal profiles and the ISA-1976 atmosphere.

Water vapor mixing ratio is computed following Bolton (1980) as it was presented in Eq. 5.10 and Eq. 5.11, assuming that the specific water vapor q_v and the water mixing ratio are equivalent.

As it has been explained in other parts of the thesis, clouds are represented by five hydrometeors within the model: cloud droplets, ice crystals, snow, rain and graupel mixing ratios, depending on the configured microphysics scheme. Nevertheless, these variables can not be inferred by the information available in a sounding. For this reason, only cloudless sky scenarios are considered in the following experiments and cloudy scenarios will be analyzed in a future work with other sources of data as cloud radar profilers, for instance.

The selection of the cloudless situations is based on a simple clear-sky index defined for the purposes of these experiments as the ratio between the DHI and GHI and setting a threshold of 0.7. This value is completely arbitrary after some trial and error tests. However, it is enough for identifying the cloudless days required here.

Regarding the vertical configuration, a set of 80 η levels are defined by using the automatic distribution function in the model software to emulate the structure that is typically used in real WRF-ARW simulations. It is performed using the algorithm available in the routine compute_eta stored at module_initialize_real.F in the folder WRFV3/dyn_em. These vertical levels are transformed into pressure levels setting the top of the model at 10 hPa and the surface pressure varying day by day using the surface values provided by the BSRN network. The IGRA soundings are linearly interpolated in terms of the $\log(p)$ to each pressure level defining the meteorological variables at half and full levels.

In this vertical configuration, the TOM and truncation errors are relatively low as it is derived from Tables 5.2 and 5.4. Therefore, they can be assumed as a higher order contribution, leading Eq. 4.3 to

$$\epsilon = f - o = \epsilon_{phys} + O(2) \sim \epsilon_{phys}. \tag{6.1}$$

Following the method used in the previous chapter, the direct forcing of aerosols is not considered in this experiment. On the one hand, there are other scientific groups dedicated to this field as it was explained before and, on the other hand, the different approaches used by each parameterization make it difficult a systematic comparison between all of them, the main interest of the current chapter.

As it was noted in Sect. 4.2.1, the shortwave schemes need two kind surface information: i) surface weather variables and ii) surface albedo. Generally, these sites contribute to the SYNOP station network. For LIN, PAY and TAM (Table 6.1) variables are encoded following the FM 12-X SYNOP codification fully described in WMO (1995). The other stations (i.e. GVN, SAP and SYO) are provided in a tabulated format and a decoding process is not required. The surface albedo is evaluated using the static data provided by the University Corporation for Atmospheric Research (UCAR) for the WRF Preprocessor System (WPS). This albedo data-set consists in a 0.144x0.144° grid spatial resolution with a monthly temporal division. Values at each site are determined following a simple bi-lineal spatial interpolation.

The main limitation of the proposed methodology is the representation of the vertical column. Generally, the sounding measurements are assumed as instantaneous and characteristic of the vertical profile at the launching coordinates. In practice, the ascent may take more than

90 min and the balloon can experience a horizontal drift exceeding 200 km due to the wind conditions (McGrath et al., 2006). However, the largest uncertainties are associated with the upper levels of the atmosphere having a low contribution to the flux attenuation and scattering due to the low air density. Another issue is when the balloon travels through a cloud in a day detected as a cloudless sky at the BSRN site. This problem has a low frequency and it is solved filtering the results before the discussion (i.e. high/low modeled DHI/DIF versus a low/high real DHI/DIF).

The discussion of the results is split in two parts. In the first part (Sect 6.2), an analysis of the ϵ_{phys} for the surface irradiances is presented. The GHI, DHI and DIF are validated defining two metrics: the normalized bias (nBias) and the normalized Mean Absolute Error (nMAE).

The nBias is defined as

$$nBias = \frac{1}{N}\sum_{i=1}^{N}\frac{f_i - o_i}{S_{0,i}\mu_{0,i}}, \tag{6.2}$$

where f_i and o_i are the modeled and real values, respectively, for the ith study case, N is the total number of cloudless cases, $S_{0,i}$ is the solar constant and $\mu_{0,i}$ is the cosine of the solar zenith angle. The experiments are performed in a single time stamp (i.e. 00 or 12 UTC) depending on the site (Table 6.1).

The nMAE is defined as a similar manner but considering the absolute differences as

$$nMAE = \frac{1}{N}\sum_{i=1}^{N}\frac{|f_i - o_i|}{S_{0,i}\mu_{0,i}}. \tag{6.3}$$

Both metrics are normalized to facilitate the comparison between sites at different latitudes. However, the scatter-plots of real vs modeled values presented in the next section are not normalized because they are used for discussing the seasonal variations of the results.

Due to the relation between the components of the flux given by

$$GHI = DHI + DIF, \tag{6.4}$$

the nBias of each variable should respond to the relationship given by

$$nBias_{GHI} = nBias_{DHI} + nBias_{DIF}. \tag{6.5}$$

In practice, this equality is not true because the components of the flux are derived from different instruments.

In the second part (Sect. 6.3), the vertical profiles of the radiative fluxes (i.e. downward direct, downward diffuse and upward diffuse) and of the heating rate of each scheme at each site are discussed. As the fluxes and heating rates are defined at the sigma levels that vary in time and place, they are regridded into a regular distribution of vertical levels spaced by 10 hPa. These values are normalized with respect to the incoming radiation and positive defined for a better comparison. Finally, the results at each level are averaged to simplify the discussion.

6.2 Analysis and discussion of ϵ_{phys}

6.2.1 General overview

The patterns observed for the GHI, DHI and DIF are consistent with those discussed in Ruiz-Arias et al. (2013) using full simulations for New Goddard and RRTMG.

With the exception of Dudhia, the GHI shows good skills with a small nBias for all the schemes and sites ranging between ∼-0.5% and 4.5% (Table 6.2). This behavior is a consequence of the balance out of an overestimation in the DHI (from 4.0% to 13.0%, Table 6.3)

and a high underestimation of the DIF (from ∼-9% and ∼-3%, Table 6.4). In Dudhia, the GHI is always underestimated with an nBias ranging from -9.1% to -0.3%.

The comparison between different solar schemes reveals a similar performance between the GHI (Fig. 6.1) and DHI (Fig. 6.2) at all the analyzed sites, while the largest departures are experienced in the DIF component (Fig. 6.3). The similarity between GHI and DHI is expected because in a cloudless scenario the direct component is the major contribution to the global irradiance.

Geographically, we find similar behaviors at sites with the same climate features. The lowest errors are experienced in the Antarctic stations (i.e. GVN and SYO) while the largest departures are reached at mid-latitude sites (i.e. PAY, LIN and SAP). As detailed in Sect. 6.1, Antarctica is the region with the lowest contribution of continental aerosols. Moreover, there is practically no ground-level aerosol production because the surface is covered by ice and snow and the water vapor content tends to be low as a result of the cold temperatures leading to a lower radiative absorption in the near-IR region of the spectrum. Consequently, the real atmosphere is more transparent and it produces a lower scattering than in other places in the world, reducing the error in the DHI and DIF fields. In contrast, mid-latitude sites require a more complex discussion due to the overlap of many factors as the water vapor and the local aerosol features.

TAM is an intermediate station with a high seasonal impact due to the Saharan effects and the African Monsoon (Sultan et al., 2003; Sultan and Janicot, 2003). However, the results obtained for this site are uncompleted on account of the high turbidity and the methodology used for selecting the cloudless days: there are days in which this station experiences a high atmospheric turbidity caused by the Saharan dust entries produced by the Harmattan winds. As a consequence, the DHI decreases significantly and these days are detected as cloudy days. Therefore, these cases are excluded in the analysis but they could contribute to increase the metrics because in the current experiments aerosols are not considered.

6.2.2 GHI

With the exception of Dudhia that does not solve the RTE explicitly, all the solar schemes show similar nBias and nMAE patterns among the site (Table 6.4, Fig. 6.3). The RRTMG and CAM parameterizations exhibit the best skill with essentially identical metric values. The New Goddard and Goddard schemes are just behind RRTMG and CAM in the performance hierarchy, with the New Goddard performing better than the original version of the scheme as would be expected. The FLG parameterization exhibited the worst performance at all sites. Dudhia will be analyzed in more detail at the end of this section.

GVN and SYO are the sites with the lowest errors being the second station slightly better than the first one. The nMAE ranges from 1.5% (RRTMG) to 2.9% (FLG) in GVN and from 1.9% (RRTMG and CAM) to 3.2% (FLG) in SYO. RRTMG and CAM produces a small underestimation of the GHI with nBias values between -0.5% and -0.0% in both sites .

In TAM, RRTMG has the best performance with a nMAE of 2.1% together with a near-zero nBias, while FLG reaches the highest nMAE with a 3.6%.

Sites located at mid-latitudes show significant differences from one station to the other due to the particularities of each region. The nMAE for RRTMG and CAM ranges between 2.3% and 2.6%, for New Goddard from 3.5% to 3.8% and for FLG from 4.3% to 4.6%. The nBias is positive in all sites (i.e. overestimating the GHI).

The Dudhia scheme is a particular case because it does not solve explicitly the RTE. Thus, this scheme only parameterizes the GHI field but not the direct and diffuse components. For this reason, this scheme is discussed separately in this section.

Using the default value for the *swrad_scat* parameter (i.e. equivalent to 10^{-5} kg m^{-2}), Dudhia shows comparable skills with respect to the other schemes at mid-latitudes sites and

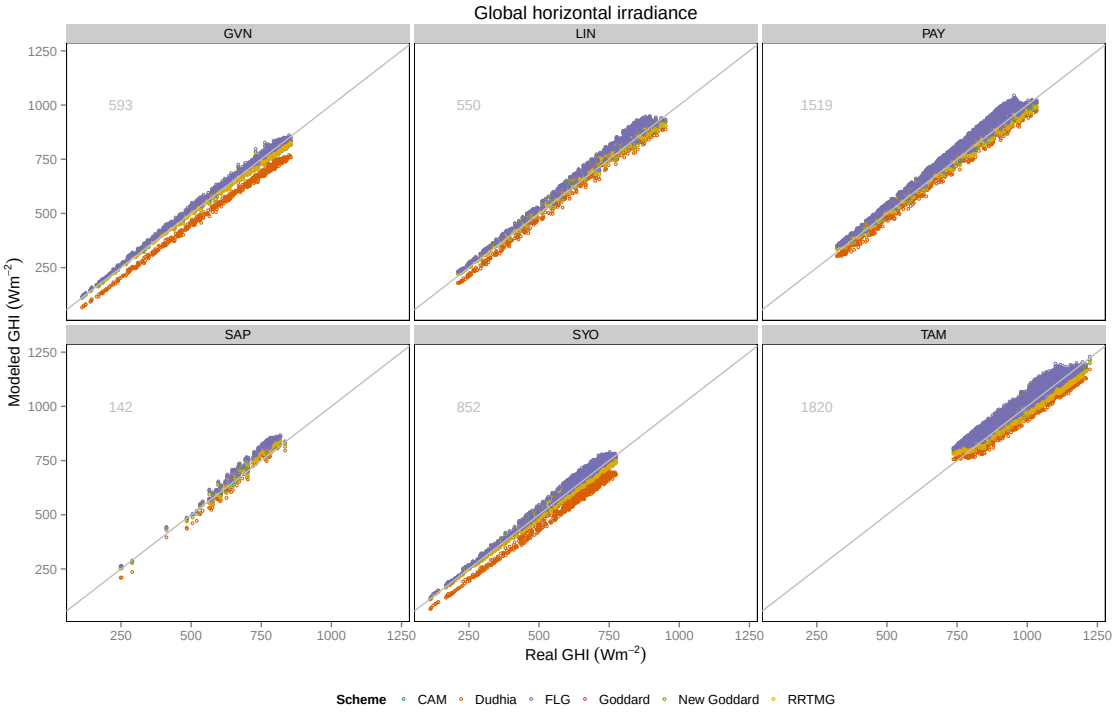

Figure 6.1: Scatter-plot showing the modeled GHI (y-axis) versus the real GHI (x-axis). Each panel represents one site. Analyzed parameterizations are indicated with different colors. The gray line shows the perfect model. The gray number indicates the number of cases analyzed.

TAM, with a slight tendency to underestimate the GHI. In constrast, this parameterization experiences the highest errors in the Antarctic sites with a significant underestimation.

In the mid-latitude sites, the nMAE ranges from 2.1% in PAY to 2.8% in LIN, while the nBias is minimum at PAY and SAP with -0.3% and maximum in LIN with -2.0%. TAM shows intermediate results with a nMAE of 2.0% and nBias of -1.3%. Finally, GVN and SYO experience a nMAE of 9.1% and 8.4%, respectively, with a negative nBias of the same magnitude. This underestimation in all sites indicates that the modeled atmosphere is more opaque than in the reality.

The parameter *swrad_scat* can be tuned for optimizing the performance of Dudhia at each site as it is shown in Fig. 6.4. All sites experience a similar pattern. When *swrad_scat* is lower than the optimal value, the modeled atmosphere is more transparent than the real, producing an overestimation of the GHI. On the contrary, for *swrad_scat* values higher than the optimal value, the modeled atmosphere becomes more opaque and the GHI is underestimated.

The optimal value for *swrad_scat* varies as a function of the geographic region reaching an asymptotic nMAE of ∼2% in all the sites. The Antarctic sites show an optimal value ∼0.5 (i.e. $5{\cdot}10^{-6}$ kg m^{-2}) consistent with the previous discussion about these sites. At the mid-latitude stations, the best configuration for *swrad_scat* varies from one site to the other ranging from 0.9 to 1.1. Finally, TAM requires a *swrad_scat* around 0.8.

6.2.3 DHI

The DHI reveals significant differences as a function of the climate region (Fig. 6.2, Table 6.3).

The RRTMG is the best parameterization in all the sites followed by the CAM and New Goddard which show similar skills. The FLG and Goddard the solar schemes with the worst results.

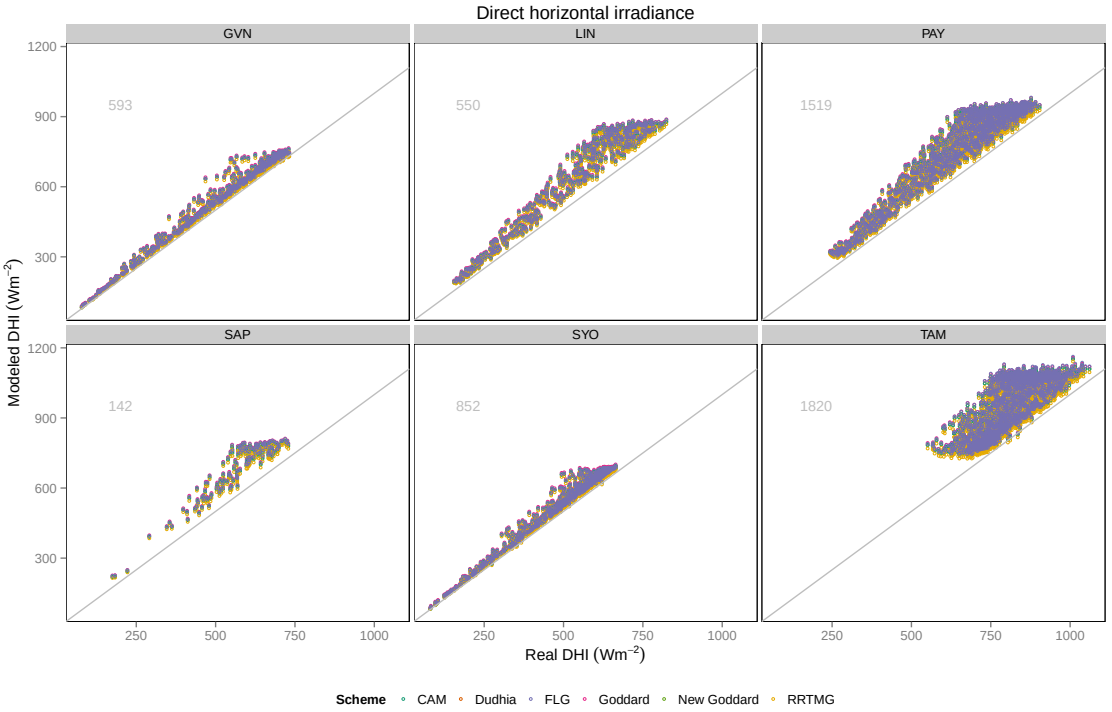

Figure 6.2: Scatter-plot showing the modeled DHI (y-axis) versus the real DHI (x-axis). Each panel represents one site. Analyzed parameterizations are indicated with different colors. The gray line shows the perfect model. Dudhia is not represented because this scheme does not solve the RTE explicitly. The gray number indicates the number of cases analyzed.

The Antarctic sites (i.e. GVN and SYO) show the lowest errors as anticipated in the discussion presented at the beginning of the Sect. 6.2.1. In both sites, the nMAE ranges from 4.0% to 6.2% as a result of a high overestimation of the direct irradiance.

In TAM, RRTMG leads to the best performance with a nMAE of 9.9%. New Goddard and CAM show a nMAE of 11.1% and the FLG and Goddard of 11.9%.

Mid-latitude sites experience the worst accuracy in the determination of the DHI. LIN and SAP show similar metrics, with LIN slightly better than SAP. The RRTMG is the best parameterization with an nMAE around 10.4% while FLG and Goddard are schemes that show the worst outcomes with a nMAE between 12.2% and 12.8%. PAY experiences better results in all schemes with a nMAE ranging from 10.4% (RRTMG) to 11.8% (Goddard).

In the context of cloudless sky conditions, the elements with the highest contribution to the attenuation of the direct solar beam are the ozone in the stratosphere, water vapor in the troposphere and aerosols. The effects due to the carbon dioxide and oxygen can be neglected because i) they have a small impact on the total flux and ii) they are assumed as a constant in space and time and therefore, they introduce a systematic contribution (Fig. 3.3). The ozone profiles have an important misrepresentation within the shortwave parameterizations (Montornès et al., 2015d), however their inaccuracies or limitations can not explain the results because we are assuming a top of the model at 10 hPa. Consequently, water vapor and aerosols are the main contributors to the errors observed in the DHI. Aerosols have an influence in the real measurements but not in the modeled values because they are not considered in this set of experiments.

The impact of the water vapor is analyzed in Fig. 6.5 for the CAM scheme. The selection of this parameterization is arbitrary but as it is demonstrated in Fig. 6.2, the following discussion is valid for the other schemes because all of them show similar behaviors. Generally, the accuracy

in DHI improves when the atmosphere has a low water content (i.e. more transparent). This is particularly prominent in the Antarctic sites in which the lowest TPW values are associated with the best skills with respect to the other sites (Table 6.3).

A similar pattern is observed for LIN, PAY and SAP. When the atmosphere has the lowest TPW values, the modeled outcomes tend to be nearer to the real value. In contrast, for higher TPW values, the DHI departures increase. This behavior is related with the seasonal patterns. The lowest TPW values occur when the DHI is minimum (i.e. winter), while the largest TPW records are observed when the DHI is maximum (i.e. summer). Thus, solar schemes tend to experience a better performance in winter than in summer.

The Saharan site (TAM) is a more complex case due to the local conditions. In general, the lowest deviations are produced when the TPW is minimum and the errors increase as the TPW is higher as in the previous sites. Nevertheless, this pattern is not observed when the modeled DHI is maximum, (i.e. summer) and hence, the TPW is higher. As it was aforementioned, TAM is located in the Sahel (southern of the Saharan desert) with a high effect of the Western African Monsoon. In the dry season (since the middle of November until the middle of May), the clear-sky days are predominant and the atmosphere shows a lower turbulence since the transport of dust from Sahara is weak (Cuesta et al., 2008) and the water vapor content is low. During the spring, the Saharan surface warms up increasing progressively the pressure gradient between the Gulf of Guinea and the continent. As a result, a convergence zone appears between the Harmattan winds and the moist monsoon flow coming from the Gulf of Guinea. This region shifts progressively to the north achieving the Sahel at the middle of May (Sultan et al., 2003; Sultan and Janicot, 2003), i.e. increasing the TPW. When the dry season finishes and the pre-onset is started, the Harmattan winds transport dust from the desert increasing the turbidity and scattering over the Tamanrasset station and decreasing the TPW. In summer, the moist monsoon flow penetrates deeply to the continent strengthening the convective systems as response to the large scale pressure gradient. The atmospheric instability favors the dust in suspension increasing the AOD (Cuesta et al., 2008) and the scattering. Finally in autumn, the Saharan surface is progressively cooled weakening the south-north pressure gradient and therefore, the monsoon flow retreats starting a transition phase to the dry season with lower water content and aerosols.

This discussion is strengthen observing the AOD at 500 nm (Fig. 6.6) provided by the Aerosol Robotic Network (AERONET, Holben et al., 1998) station at the same place. The maximum aerosol forcing is associated with the minimum TPW values and the highest errors in the DHI experienced on later spring and summer. In contrast, the lowest aerosol forcing is associated with the lowest TPW and DHI values (i.e. winter) when all the schemes produce the best results.

6.2.4 DIF

Comparing the solar schemes for any site, we observe that CAM produces the lowest scattering atmosphere while FLG is on the other extreme (Fig. 6.3, Table 6.4). RRTMG and New Goddard show similar outcomes being near to the FLG in performance, while Goddard models a slightly lower scattering atmosphere. In terms of the metrics, CAM shows the worst accuracy in all the sites with an nMAE ranging from 4.5% in SYO to near 9.0% in LIN. Finally, FLG is the best scheme producing the lowest nMAE values ranging from 2.1% in SYO to 7.3% in SAP.

The analysis of the DIF shows two well defined regions (Fig. 6.3). For low DIF real values, all the parameterizations show a good performance with a small tendency to underestimate the diffuse component. This behavior is specially well noted in the Antarctic sites where the real scattering is low. However there is a threshold at which all the schemes reach an asymptotic value with respect to the real data, modulated by the radiation features of each latitude. This pattern is specially important in TAM. LIN, PAY and SAP experience an overlapping of both behaviors.

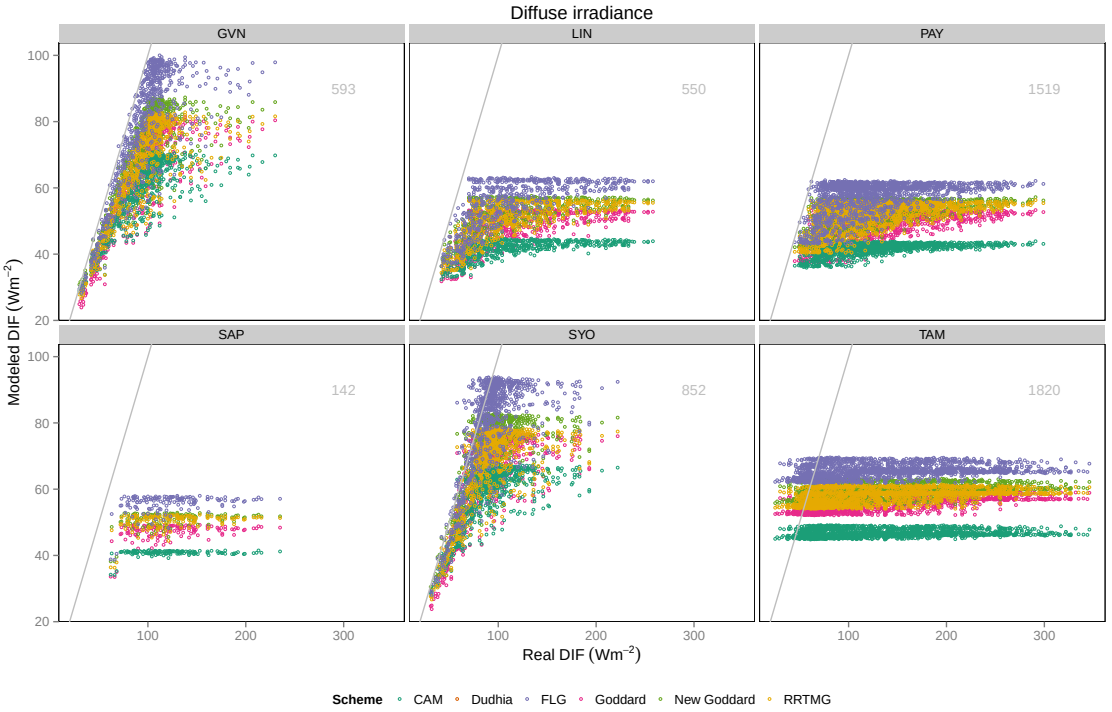

Figure 6.3: Scatter-plot showing the modeled DIF (y-axis) versus the real DIF (x-axis). Each panel represents one site. Analyzed parameterizations are indicated with different colors. The gray line shows the perfect model. Dudhia is not represented because this scheme does not solve the RTE explicitly. The gray number indicates the number of cases analyzed.

In a cloudless atmosphere, the scattering is the result of two physical processes: i) the Rayleigh scattering due to the gas molecules and ii) the Mie scattering due to the aerosols that it is not considered in this set of experiments (Sect. 6.1). Briefly, the Rayleigh scattering is parameterized in terms of a scattering coefficient as a function of the wavelength and the dry air mass composing a layer of the grid-point column. Given one site, the total dry air mass shows a low variation along the time. Therefore, the highest contribution to the DIF variation is the incoming radiation at TOA. Consequently, when the real atmosphere has a low forcing due to the aerosols (i.e. as in the Antarctic sites), the Rayleigh

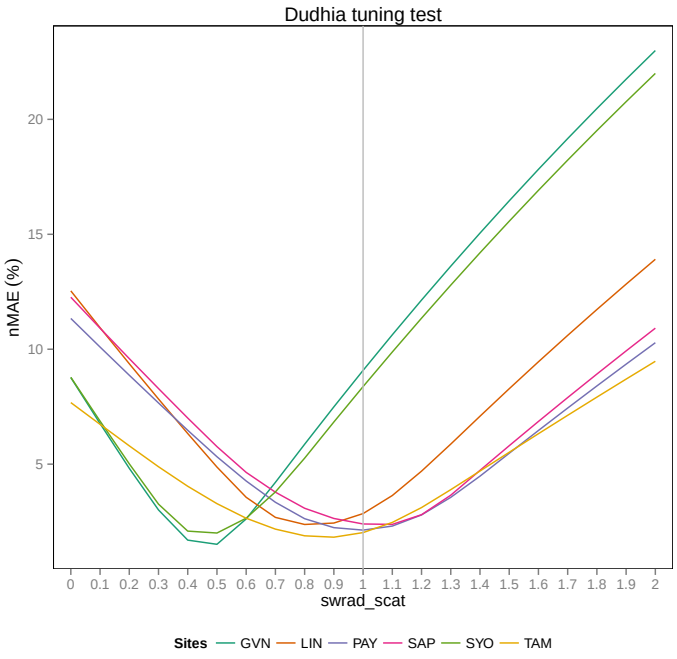

Figure 6.4: Dudhia's tuning results for a nMAE optimization. The vertical line shows the default value proposed in WRF-ARW.

scattering becomes the main contribution to the DIF component of the flux and the modeled value has a good correlation with the observations. Contrarily, when aerosols produce a significant forcing, the solar parameterizations reach the asymptotic value with respect to the observations. For this reason, the first region associated with the Rayleigh scattering is well noted in the Antarctic sites (GVN and SYO) while the problem with the aerosols is prominent in the Saharan site (TAM) as observed in Figs. 6.3 and 6.6.

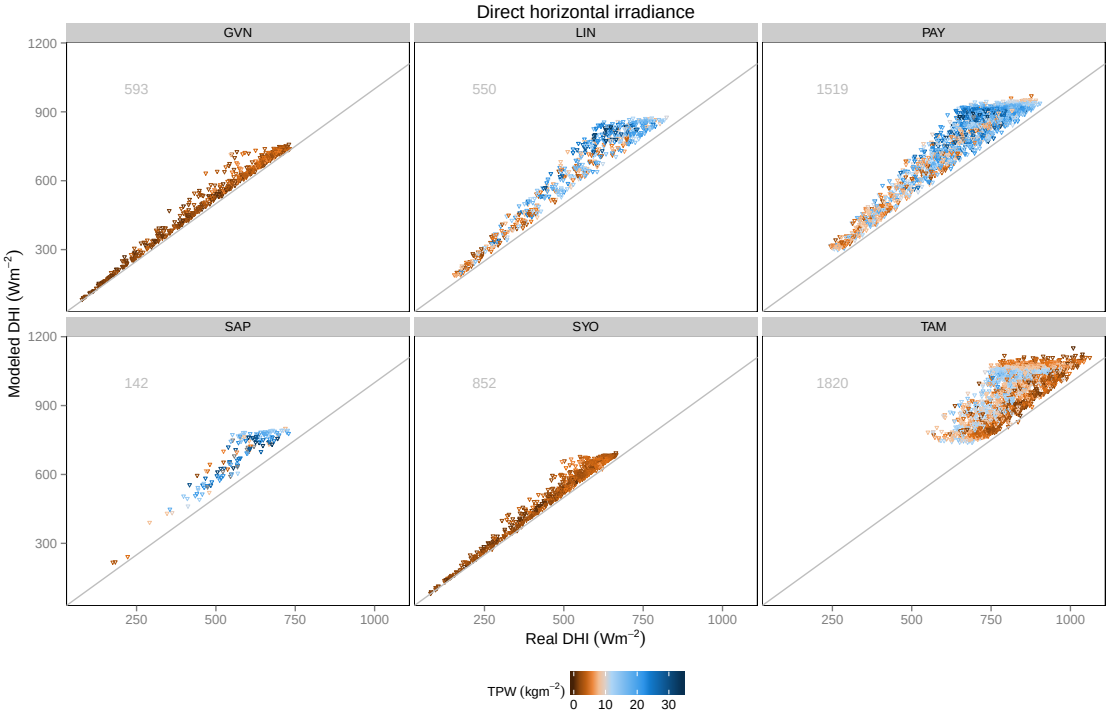

Figure 6.5: Example for the CAM scheme showing the impact of the Total Precipitable Water (TPW) on the DHI modeling. Color gradient indicates the TPW from dry days (brown) to moist days (blue). Although this figure is particular for CAM, the observed behavior can be extrapolated to the other parameterizations in virtue of Fig. 6.2. The gray line indicates the perfect model. The gray number indicates the number of cases analyzed.

A secondary factor that modulates these errors is the surface albedo as it will be detailed in Sect. 6.3.

6.3 Physical discussion of the modeled fluxes and heating rate profiles

In this section, we present a discussion about the behavior of the radiative fluxes and heating rate in the vertical. In the analysis of the fluxes, the results for the downward direct, downward diffuse and upward diffuse are presented. For this reason, Dudhia is not included. In the second part, all the parameterizations are analyzed even though it is necessary to remember that Dudhia does not solve the RTE and hence, the heating rate is not defined as the divergence of the flux.

The vertical profiles of the shortwave fluxes show similar patterns at each site (Fig. 6.7). The Beer's law governs the behavior of the direct flux. The solar direct beam is maximum at TOA and decays across the atmosphere as a function of optical thickness that is parameterized in terms of the atmospheric components. Therefore, two different behaviors are observed: one in the lower/mid troposphere and the other in the upper troposphere. The upper troposphere

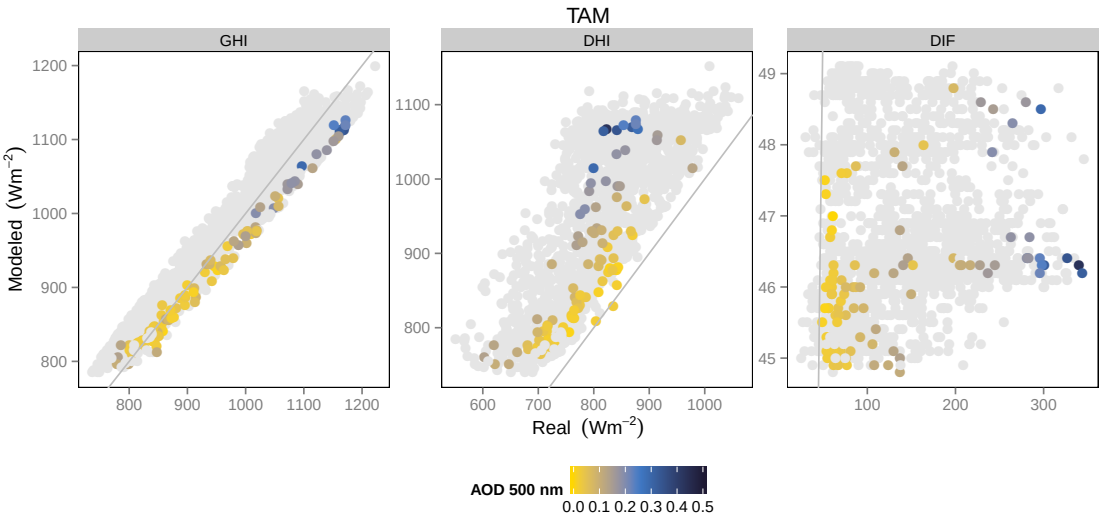

Figure 6.6: Example of the impact of the real aerosols on the CAM scheme errors at TAM. The Aerosol Optical Depth (AOD) at 500 nm loaded from the AERONET, (level 2.0) is represented in colors. Gray points are days without available measurements. Although this figure is particular for CAM, the discussion can be extrapolated to the other parameterizations in virtue of Figs. 6.1, 6.2 and 6.3.

Table 6.2: GHI averaged metrics for all data-sets normalized with respect to the extraterrestrial radiation

GHI [%]	TAM		GVN		SYO		LIN		PAY		SAP	
Scheme	nBIAS	nMAE	nBIAS	nMAE	nBIAS	nMAE	nBIAS	nMAE	nBIAS	nMAE	nBIAS	nMAE
Dudhia	-1.3	2.0	-9.1	9.1	-8.4	8.4	-2.0	2.8	-0.3	2.1	-0.3	2.4
Goddard	2.6	3.0	1.5	1.9	1.9	2.3	3.7	3.8	3.9	4.1	3.9	4.0
New Goddard	2.2	2.7	1.4	1.8	1.7	2.2	3.3	3.5	3.6	3.8	3.5	3.7
CAM	1.1	2.2	-0.3	1.7	0.0	1.9	1.7	2.3	2.1	2.6	2.0	2.6
RRTMG	0.8	2.1	-0.5	1.5	0.0	1.9	1.8	2.3	2.1	2.6	2.0	2.6
FLG	3.4	3.6	2.8	2.9	3.1	3.2	4.2	4.3	4.5	4.6	4.5	4.5

Table 6.3: DHI averaged metrics for all data-sets normalized with respect to the extraterrestrial radiation

DHI [%]	TAM		GVN		SYO		LIN		PAY		SAP	
Scheme	nBIAS	nMAE	nBIAS	nMAE	nBIAS	nMAE	nBIAS	nMAE	nBIAS	nMAE	nBIAS	nMAE
Dudhia	-	-	-	-	-	-	-	-	-	-	-	-
Goddard	11.9	11.9	6.2	6.2	6.2	6.2	12.8	12.8	11.8	11.8	12.8	12.8
New Goddard	11.1	11.1	5.2	5.2	5.2	5.2	11.8	11.8	11.1	11.1	12.0	12.0
CAM	11.1	11.1	5.2	5.2	5.1	5.1	11.4	11.4	10.7	10.7	11.6	11.6
RRTMG	9.9	9.9	4.0	4.0	4.0	4.0	10.4	10.4	10.4	10.4	10.5	10.5
FLG	11.9	11.9	5.7	5.7	5.5	5.5	12.2	12.2	11.6	11.6	12.5	12.5

Table 6.4: DIF averaged metrics for all data-sets normalized with respect to the extraterrestrial radiation

DIF [%]	TAM		GVN		SYO		LIN		PAY		SAP	
Scheme	nBIAS	nMAE	nBIAS	nMAE	nBIAS	nMAE	nBIAS	nMAE	nBIAS	nMAE	nBIAS	nMAE
Dudhia	-	-	-	-	-	-	-	-	-	-	-	-
Goddard	-6.6	6.7	-4.6	4.6	-3.7	3.7	-8.2	8.2	-7.8	7.8	-8.2	8.2
New Goddard	-6.3	6.4	-3.7	3.7	-2.9	2.9	-7.6	7.6	-7.4	7.4	-7.8	7.8
CAM	-7.4	7.4	-5.3	5.3	-4.5	4.5	-8.8	8.8	-8.5	8.5	-8.9	8.9
RRTMG	-6.5	6.6	-4.3	4.3	-3.4	3.5	-7.8	7.8	-7.5	7.5	-7.9	7.9
FLG	-5.8	6.1	-2.7	2.7	-1.8	2.1	-7.1	7.1	-6.9	6.9	-7.3	7.3

(i.e. p $\leq$ 250 hPa) is practically transparent with an attenuation around $\sim$10%. This is because of the low air density, although the absorption due to ozone at the UV region of the spectrum (Fig. 3.3). On the contrary, the direct beam decreases faster in the mid and lower troposphere due to the higher air density and the absorption experienced by water vapor in the near-IR bands and the scattering produced by a higher air density near to the ground. The analysis indicates that the RRTMG produces the least transparent atmosphere at all sites while Goddard scheme simulates the most transparent atmosphere.

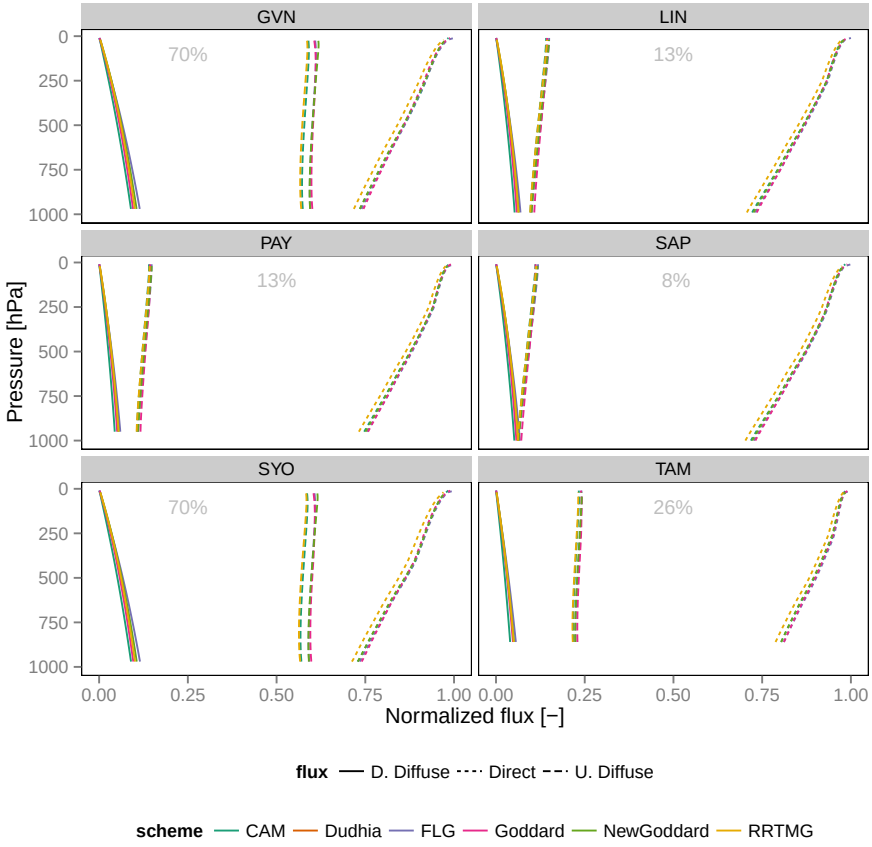

Figure 6.7: Vertical profile of the averaged shortwave fluxes: downward direct, downward diffuse and upward diffuse. Values are normalized with respect to the incoming radiation at TOA. The number in gray indicates the averaged albedo.

The diffuse downward flux shows a similar behavior site by site since the only scattering element considered in these experiments is the Rayleigh scattering. In the upper atmosphere, all the schemes show near-zero values. The differences among the schemes are larger in the lower troposphere with the FLG scheme generating the most scattering and the CAM and Goddard parameterizations exhibiting the lowest scattering.

The magnitude of the upward diffuse flux is strongly dependent on the site because of the significant variations in surface albedo. GVN and SYO, with an averaged albedo of 70%, show the highest mean upward diffuse flux at the surface of around 0.6 with respect to the incoming radiation and TOA. TAM has an averaged albedo of 26% producing an intermediate diffuse upward flux $\sim$0.2 with respect the incoming radiation. PAY and LIN, both have an averaged albedo of 13% leading to values around 0.12 at the ground. Finally, SAP has an averaged albedo of 8% becoming the site with the lowest diffuse upward flux at the surface. As a consequence of the multiscattering processes represented for example by the Adding method, a higher diffuse upward flux due to the albedo produces a higher diffuse downward flux reducing

the nBias of the DIF in the Antarctic sites.

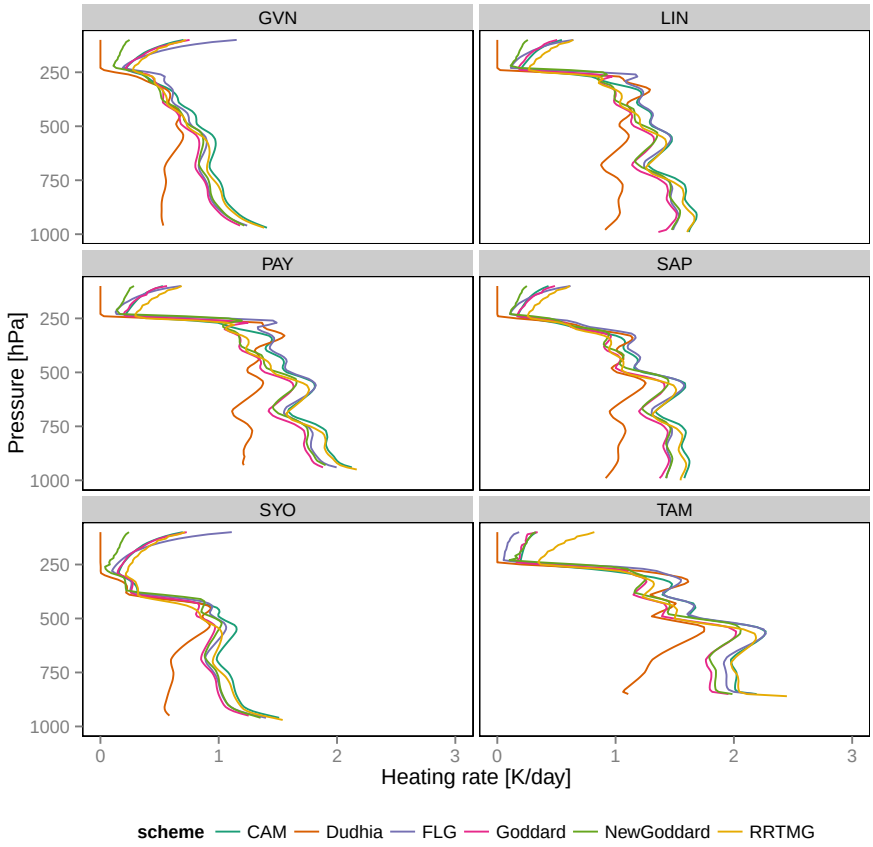

Figure 6.8: Vertical profile of the averaged heating rate in the troposphere

The vertical profile of the heating rate shows important differences between the troposphere (Fig. 6.8) and the stratosphere (Fig. 6.9) in the behavior as well as in the magnitude. In the troposphere, the heating rate experiences rough variations with the height ranging from 0 to $\sim$2 K day^{-1}. These deviations are associated with day-to-day differences in the water vapor profile. Thus, the Antarctic sites show the smoothest behavior. On the contrary, the heating rate in the stratosphere ranges from 1 to 4 K day^{-1} and even 8 K day^{-1} for FLG with smoother variations with the height as a consequence of the climate ozone profiles used by the schemes (Montornès et al., 2015d).

Below 750 hPa, CAM and RRTMG are the schemes that experience more radiative absorption. Goddard and New Goddard have similar results even though New Goddard produces a slightly higher absorption. These differences are associated with variations in the treatment of the water vapor (Fig. 3.3). Dudhia is the parameterization with the lowest absorption with $\sim$1 K day^{-1} less than the others in the troposphere.

The Antarctic sites experience the lowest heating rates with a fast reduction with height. In GVN, the heating rate is significantly lower than in SYO linked with lower TPW values (Fig. 6.5). The heating rate in Dudhia ranges from 0.5 to 0.6 K day^{-1}. Goddard, New Goddard and FLG produce similar average heating rates with values between 1.3 and 0.9 K day^{-1}. Finally, the heating rates produced by CAM and RRTMG schemes range from 1.4 to 1.0 K day^{-1}.

Mid-latitudes sites show a low variation with the height in the low troposphere. In LIN and SAP, the heating rate ranges from $\sim$1 K day^{-1} in Dudhia to $\sim$1.6 K day^{-1} in CAM and RRTMG. The other schemes show intermediate values around 1.4-1.5 K day^{-1}. In PAY, the

heating rate is around 1.2 K day^{-1} for Dudhia while the remaining schemes range from 1.7 to 2 K day^{-1} even higher at the first layers.

Finally, TAM shows the highest heating rate values from 1.1 K day^{-1} for Dudhia to 2.4 K day^{-1} for the RRTMG.

In the middle troposphere (i.e. from 750 to 300 hPa) the heating rate tends to become lower at all the sites and for all the schemes. The Antarctic sites show a heating rate lower than 1 K day^{-1} while the mid-latitude and Saharan sites produce a heating rate between 1 K day^{-1} and 1.5 K day^{-1}. The heating rates continue decreasing until reaching zero or near-zero values around 250 hPa. From this height, the heating rate increases again smoothly with the exception of Dudhia that remains at zero as a consequence of the omission of the ozone absorption.

In the stratosphere, the heating rate increases from ∼1 K day^{-1} to 3-4 K day^{-1} excepting Dudhia and FLG. The first one experiences zero values because it does not consider the ozone (Fig. 3.3), while the second one produces higher values than the other schemes, ranging from ∼7 to ∼13 K day^{-1}. The other schemes yield similar results with New Goddard parameterization producing the lowest absorption. The results for Dudhia, New Goddard, CAM and RRTMG are consistent with those observed in Montornès et al. (2015e) using real WRF-ARW simulations. Goddard and FLG were not discussed in that study.

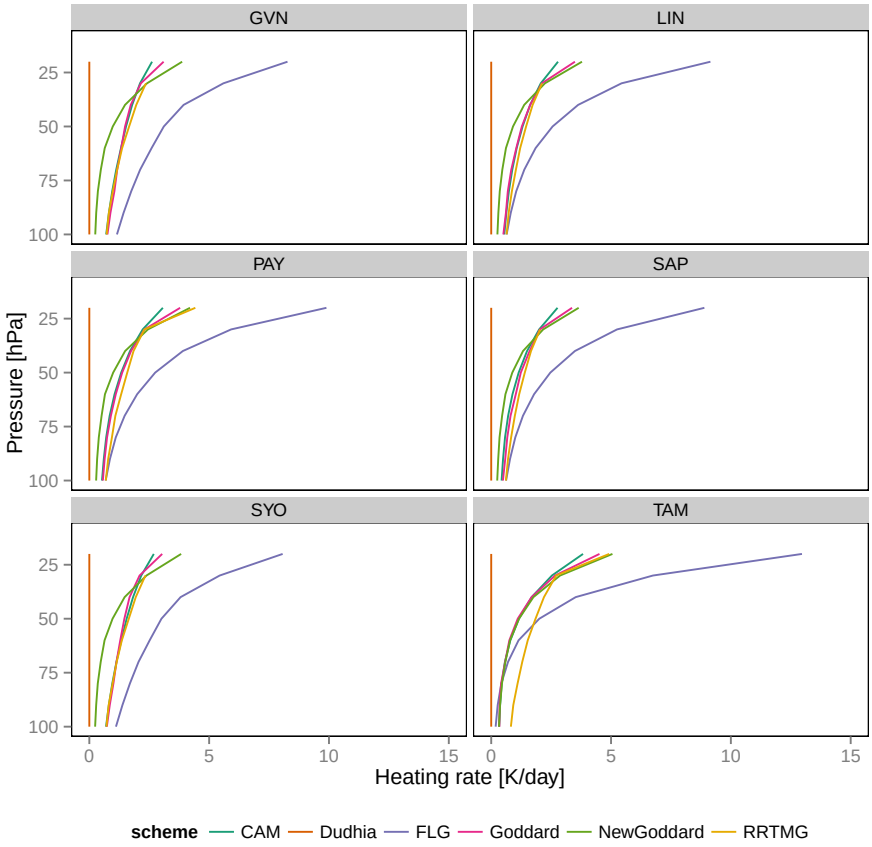

Figure 6.9: Vertical profile of the averaged heating rate in the stratosphere